RSC Advances

PAPER

View Article Online
View Journal | View Issue

Cite this: *RSC Adv.*, 2024, **14**, 6048

Effect of lead-free glass on the current transmission method at the Ag/Si interface in crystalline silicon solar cells

Hu Sun, [a] Xianglei Yu,[a] Siqi Quan,[a] Weichao Li,[b] Zhuo Qian,[a] Junpeng Li*[c] and Guoyou Gan*[a]

Received 17th January 2024
Accepted 9th February 2024

DOI: 10.1039/d4ra00456f

rsc.li/rsc-advances

Environmental protection mandates have spurred the widespread adoption of lead-free glass in electronic material adhesion. Glass powder, crucial for solar silver paste, notably affects the ohmic contact at the Ag–Si interface of crystalline silicon solar cells. This study examines how TeO_2 content influences the high-temperature flowability and wettability of lead-free Bi_2O_3–TeO_2-based glass powder, alongside the interplay between the glass's thermal properties and interface contact. Additionally, it investigates the Bi_2O_3–TeO_2 ratio's impact on current transmission through the interfacial glass layer. Experimental results show that the synthesized glass powder exhibits superior high-temperature flowability and wettability, with a low contact resistance of 1.5 mΩ cm^2 in silver paste applications. This study also proposes an optimal approach for enhancing current transmission through the interfacial glass layer. Consequently, this glass powder is highly valuable for c-Si solar cell silver paste applications, offering novel insights into improving current transmission efficiency.

1. Introduction

The swift advancement of clean energy has significantly heightened interest in crystalline silicon solar cells in recent years. Specifically, electronic paste, used in the front silver paste of c-Si solar cells, is of particular significance.[1,2] Glass powder, acting as an adhesive in the front silver paste of c-Si solar cells, is crucial in the front electrode's metallization process.[3] The glass etches the anti-reflective coating and establishes ohmic contacts, influencing the electrode's sintering process and electron conduction mechanism.[4–6] In other words, glass significantly influences interface contact resistance, a key contributor to energy loss in the electron transmission of c-Si solar cells.

Bi_2O_3 and TeO_2, being environmentally benign, are increasingly used in c-Si solar cell silver paste as alternatives to traditional PbO glass.[7,8] In lead-free glass research, the combination of Bi_2O_3 and TeO_2 glass, due to their similar properties to traditional PbO glass and lower thermal performance, respectively, has become a central focus in glass powder studies.[8–10] Hui Wang *et al.* investigated Te-modified lead-free glass, discovering that it forms a dense surface upon melting and lowers the contact angle with silicon wafers, thereby enhancing wettability.[11] Hyungsun Kim *et al.* noted that TeO_2/(TeO_2 + PbO) glass shows an increased likelihood of recrystallizing on silicon nitride layers, leading to reduced ohmic contact resistance.[12] Yun Chan Kang *et al.*'s research suggests that the Bi_2O_3 in Bi-based glass powder enhances the silver paste's sintering characteristics and the glass's thermal stability.[13]

Numerous researchers have intensively investigated the complexities of the firing process in lead-free crystalline silicon solar cells' front silver paste and their electrical contact with silicon.[14] When the sintering temperature exceeds the glass's melting point but remains below that of the silver powder, the molten glass flows through the silver powder gaps to the Ag–Si interface, initiating an etching reaction.[15] Silver ions in the paste dissolve into the glass and diffuse towards the silicon emitter's surface, where they are reduced at the etched sites, forming silver crystals. In the cooling process, the oversaturated silver within the glass precipitates out as particles, forming a complex contact layer on the pyramid-textured silicon surface. Xiaolong Du *et al.* employed selective acid etching and mechanical exfoliation to directly observe the silicon emitter interface layer. They proposed four Ag–Si contact types and current transmission paths: direct pathways *via* silver microcrystals, indirect routes through Ag microcrystals and particles, direct single-step tunneling from the Si emitter to the silver block, and a multi-step tunneling effect from the Si emitter to the silver block.[16] G. Schubert *et al.* used *in situ* R_c measurements to discover that direct contact with silver microcrystals

[a]*Faculty of Material Science and Engineering, Kunming University of Science and Technology, Yunnan Province, 650031, People's Republic of China. E-mail: ganguoyou@kust.edu.cn*

[b]*R&D Center of Yunnan Tin Group (Holding) Co., Ltd., Yunnan Province, 650200, People's Republic of China*

[c]*Sino-Platinum Metals Co., Ltd., Yunnan Province, 650106, People's Republic of China. E-mail: lijunpeng@ipm.com.cn*

results in extremely low contact resistivity.[17] C. H. Lin *et al.* utilized transmission electron microscopy to examine the interface structure of screen-printed silver contacts on c-Si solar cells, identifying the Ag bulk/thin glass layer/Si contact as the crucial pathway for current transmission.[18] Although these studies elucidate the interface contact methods and current transmission paths, they do not extensively explore how glass influences these contacts and the forms of Ag in the glass layer. Thus, this research aims to control interface contact methods by modifying the glass composition, ultimately improving current transmission efficiency.

In this study, we synthesized the TeO_2–Bi_2O_3–B_2O_3 lead-free glass systems. We controlled the glass's high-temperature flowability and wettability within this systems by adjusting the TeO_2 ratio. This step is critical because TeO_2 can improve the glass's low thermal properties, essential for the interfacial contact properties of silver paste.[7,14] Additionally, employing mechanical exfoliation for sample preparation and selective acid etching, we directly observed the interface contact methods, glass phase distribution, and silver microcrystals and particles on/in the silicon emitter and interfacial glass layer *via* SEM. We conducted an in-depth study on the correlation between the glass samples' thermal properties and the interface contact, revealing how the glass composition ratio affects the growth of silver microcrystals on the silicon emitter and the formation of silver particles in the interfacial glass layer. We proposed an optimal interfacial contact method, leading to glass samples for silver paste with reduced contact resistance. Overall, this research clarifies the impact of glass properties on interface contact methods and current transmission paths, offering vital guidance for developing high-performance glass powders for future solar cell applications.

2. Experimental

2.1 Materials

This study utilized semi-processed crystalline silicon solar cells measuring 182 mm × 182 mm with a sheet resistance of 80 Ω sq^{-1}, treated using aluminum back-field technology. The glass powder was prepared using the following chemical raw materials: Bi_2O_3 (≥99.5%, Zhengzhou PainI), TeO_2 (≥99.0%, Tianjin Yaohua), B_2O_3 (≥99.5%, Tianjin Fuchen), Al_2O_3 (≥99.5%, Tianjin Fuchen), and ZnO (≥98.5%, Tianjin Kaitong). The organic carrier was prepared using these chemical raw materials: ethyl cellulose (Aladdin), diethylene glycol dibutyl ether (≥98%, Aladdin), and rosin alcohol (≥98%, Aladdin). The silver powder for the silver paste, with an average particle size of about 1 μm, was sourced from Sino-Platinum Metals Co., Ltd. The solar screen mesh for screen printing was procured from Kunshan Silk Screen Products Co., Ltd.

2.2 Preparation of glass frit

This study employed the melt-quenching method to prepare the glass powder. Using the components listed in Table 1, we accurately weighed the necessary oxides for each formula. The uniformly mixed raw materials were ground in a mortar until homogeneous and then transferred into a new alumina crucible. The crucible with reactants was placed in a muffle furnace and calcined at 1300 °C to ensure complete reaction of the liquefied mixture. Subsequently, the molten glass was rapidly poured into deionized water, yielding clear yellow glass particles. The dry glass particles were then mixed with ethanol and subjected to wet ball milling at 300 rpm for 24 hours. Finally, a 400 mesh sieve was used to screen the glass powder, obtaining samples with the desired particle size.

Table 1 Compositions of the glass system (wt%)

Sample	Bi_2O_3	TeO_2	B_2O_3	Al_2O_3	ZnO	Other
G1	60	5	20	3	2	10
G2	50	15	20	3	2	10
G3	40	25	20	3	2	10

2.3 Preparation of cylindrical models

The glass powder was uniformly mixed with anhydrous ethanol in a 90 wt% : 10 wt% ratio to create a paste with optimal viscosity and dispersity. A cylindrical tablet press mold (size: 5 mm, model: HF-5, depth: 20 mm, material: CR12) was used, and 0.2 g of the sample was evenly distributed between two pads in the mold cavity. The press rod was inserted and gently rotated to flatten the sample, thus preventing damage to the mold walls from uneven pressure. The mold was positioned in the center of the tablet press workbench, and the tablet press screw was tightened to apply a pressure of 1 MPa to the sample for 60 s.[19] Finally, the cylindrical sample (diameter: 5 mm, height: 6 mm) was removed and positioned on a silicon wafer. The sample was subsequently heated in a muffle furnace at temperatures of 400 °C, 500 °C, 600 °C, 650 °C, 700 °C, and 800 °C for 90 seconds at each temperature.

2.4 Screen printing of Ag paste

The silver powder, specific organic carrier, and various glass powders (G1, G2, G3) were mixed in an 88/10/2 wt% ratio and processed using a three-roll mill. The final front gap of the three-roll mill was set to 3 μm, and the rear gap to 5 μm, producing a series of silver pastes with various glass powders (P1, P2, P3). The prepared silver pastes were screen-printed onto the solar silicon wafers, then placed in a forced-air drying oven at a constant 160 °C for 20 minutes, followed by sintering in a chain infrared furnace at a maximum temperature of 830 °C. Ultimately, c-Si solar cells were successfully fabricated, with the cells made using different silver pastes labeled as C1, C2, and C3.

2.5 Preparation of interface samples

The c-Si solar cell samples were transformed into longitudinal cross-sectional samples using mechanical grinding. Subsequently, the c-Si solar cell samples were sequentially immersed in HNO_3 and HF solutions, with rinsing and drying after each immersion. In the first step, concentrated HNO_3 solution was used to remove the surface silver electrodes and directly connected silver particles, exposing the glass layer surface. In the

second step, the glass layer surface samples were treated with 5 mol per L HF solution to remove the glass layer and any silver particles not adhered to the silicon surface, resulting in silicon surface samples.[20–22]

2.6 Characterizations

Crystal structures of the glass frits were investigated by X-ray diffraction (XRD, Rigaku, Ultima IV) with Cu Kα radiation. The thermal properties of the glass powder were measured with a simultaneous thermal analyzer (TG-DSC, Netzsch, STA409C) across a temperature range of 25 to 850 °C at a heating rate of 10 °C min^{-1}. X-ray photoelectron spectroscopy (XPS, ULVAC-PHI, PHI5000, VersaProbe III) was used to analyze the elements and valence states of different glass powders. A contact angle meter (SL200KS, USA KINO Industry Co.) was used to observe the thermal changes in different glasses with temperature and the contact angles between molten glasses and silicon wafers. Microscopic images of samples prepared through selective chemical etching and mechanical grinding were captured using a scanning electron microscope (SEM, HITACHI-SU8010, Hitachi Instruments). The resistance between silver electrodes was measured with a digital DC resistance meter (VC4090A, China VICTOR) to determine the contact resistance R_c. The *I–V* performance of the solar cell samples was assessed using a Halm instrument.

3. Results and discussion

XPS spectroscopy was used to analyze the elemental composition and valence states of the glass powder, as depicted in Fig. 1. Fig. 1(a) shows the full XPS spectrum of the glass powder, revealing the presence of Bi, Te, B, Zn, and Al, while Fig. 1(b) presents the XPS spectrum of the C element. The C element is present as C–C single bonds (binding energy: 284.8 eV) and C=O double bonds (binding energy: 289.31 eV), with the C–C single bond peak used for calibration. Fig. 1(c) illustrates that Bi in the XPS spectrum exhibits binding energies of 159.18 eV and 164.58 eV. Fig. 1(d) shows the XPS spectrum of Te, featuring two peaks at binding energies of 576.10 eV (Te $3d_{5/2}$) and 586.58 eV (Te $3d_{3/2}$). Te is present in the glass in a tetravalent state without any change in valence. Fig. 1(e) and (f) indicate the binding energy of B 1s at 191.58 eV, and O 1s at 531.33 eV. Consequently, the chemical states of the oxides in the glass powder remained unchanged during the preparation process, confirming their chemical stability.

The lead-free glass powders were analyzed using X-ray diffraction (XRD), as depicted in Fig. 2(a). The XRD patterns of the three glass powder samples, namely G1, G2, and G3, reveal a prominent broad peak at approximately 28°, characteristic of an amorphous structure, indicating that the G1, G2, and G3 glass powders are all uniform amorphous glasses. DSC analysis was conducted to evaluate the thermal properties of lead-free glass, as illustrated in Fig. 2(b). Table 2 presents data on the glass transition temperature (T_g), onset crystallization temperature (T_c), melting temperature (T_m), and their difference ΔT ($\Delta T = T_c - T_g$) for the lead-free glass. The three prepared types of lead-free glass all showed lower transition temperatures, advantageous for early-stage sintering softening and enhancing silver dissolution in the glass to improve conductivity. The ΔT values for the glasses are 118.1 °C, 117.3 °C, and 121.3 °C, respectively, suggesting good thermal stability for each type. The melting temperature (T_m) is the temperature at which the glass melts. A lower T_m in lead-free glass aids in earlier flow during sintering, enhancing SiN_x etching for better contact. As indicated in Table 2, with increasing TeO_2 content in the glass, the melting temperature of the lead-free glass initially increases and then decreases, consistently maintaining a relatively low level.

The glass powder was formed into cylindrical shapes using a tablet press mold and placed on c-Si solar cell samples measuring 20 mm × 20 mm. Fig. 3 displays the morphologies of different glass samples at temperatures ranging from 400 to 800 °C. Fig. 4 illustrates the wetting angles between various glasses and silicon wafers when the glasses are fully melted. With increasing temperature, the morphology of all samples starts to change. Upon reaching the softening point, the samples' volume decreases, yet their cylindrical shape is maintained. As the temperature approaches the crystallization temperature, the samples start to expand and become spherical upon melting. With further temperature increase, the glass's viscosity decreases and, under gravity, the spherical shape collapses, spreading over the silicon wafer surface. In the melting process, a quicker transition from spherical to hemispherical shape indicates better high-temperature flowability of the glass.

As depicted in Fig. 3, with changing temperatures, the volume of various glass cylinders initially decreases during softening, increases at crystallization, and decreases again upon melting. Among the samples, G1 and G3 glasses have lower melting temperatures, whereas G2 has the highest. Based on the Bi_2O_3–TeO_2 binary phase diagram, the liquidus temperature increases with a Bi_2O_3 to TeO_2 mass ratio from 95 : 5 to 75 : 25 and decreases from 75 : 25 to 34 : 66.[23] The Bi_2O_3 to TeO_2 mass ratio in sample G1 is 92.3 : 7.7, in G2 it's 77 : 23, and in G3 it's 61.5 : 38.5. Consequently, G2 exhibits the highest melting temperature. G1 starts spherizing at 600 °C and fully spreads over the silicon wafer at 700 °C; G2 begins at 650 °C and also fully spreads at 700 °C; G3 follows the same pattern, spherizing and spreading at 650 °C and 700 °C, respectively. Therefore, G2 has the narrowest range from spherization to melting point (100 °C for G1, less than 50 °C for G2, and 50 °C for G3). This suggests that G2 undergoes the fastest transition from spherization to melting, indicative of its excellent high-temperature flowability. Between 700 to 800 °C, the morphology of G1 and G3 remains largely unchanged, while G2's wetting angle with the silicon wafer decreases. Fig. 4 demonstrates that after complete melting, the contact angle of G2 with the silicon wafer is smaller than those of G1 and G3 (Fig. 4(a)–(c)). As the TeO_2 content in the glass increases, the contact angle of the fully melted glass with the silicon wafer initially decreases and then increases.

The experimental results indicate that with 5–25% wt TeO_2 in the glass, the melting temperature of the lead-free glass

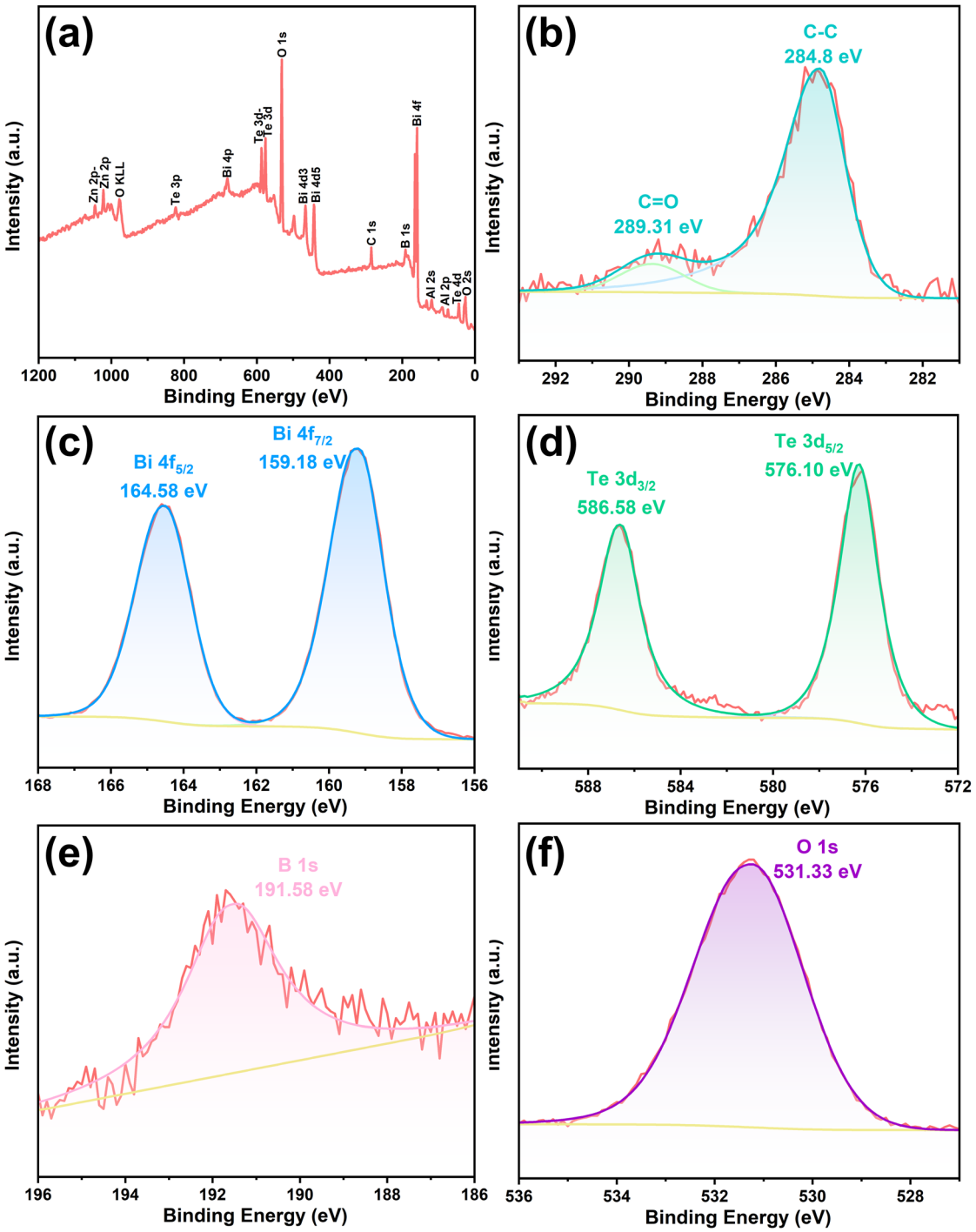

Fig. 1 (a) The X-ray photoelectron spectroscopy of G2 glass frit; (b)–(f) the X-ray photoelectron spectroscopy of elements contained in G2 glass frit.

initially rises and then falls as the TeO_2 content increases. Likewise, the glass's high-temperature flowability and wettability to c-Si solar cell wafers exhibit a similar trend of initially increasing and then decreasing. Consequently, G2 glass demonstrates superior high-temperature flowability and wettability.

In c-Si solar cells with a random pyramidal texture, the distribution of the glass layer and silver microcrystals significantly influences the interface current transmission. Fig. 5(a1)–(c1) displays SEM images showing the cross-sectional view of the front metallization of c-Si solar cells. Fig. 5(a1)–(c1) correspond to samples C1, C2, and C3, metallized with silver pastes P1, P2, and P3 made from glasses G1, G2, and G3, respectively. The cross-sectional images reveal a continuous glass layer between the Ag-bulk and the Si emitter, containing silver particles of various sizes. Additionally, the shape and

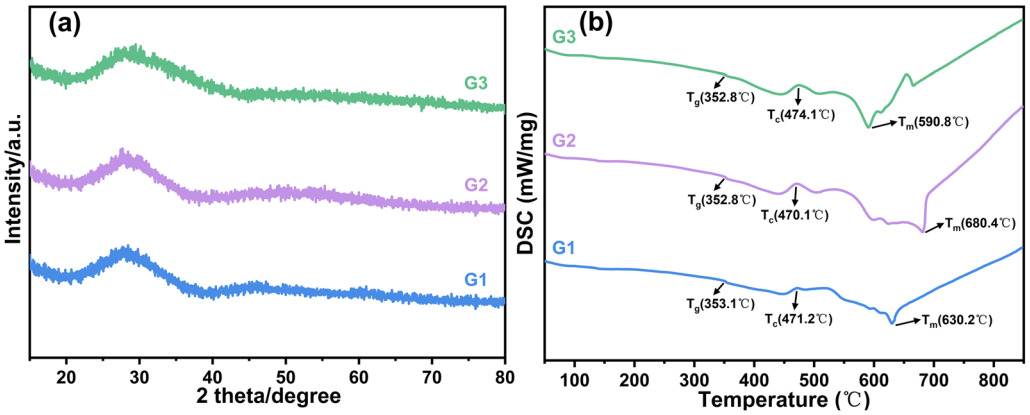

Fig. 2 (a) XRD curves of the glass samples; (b) DSC curves of the glass samples.

Table 2 Characteristic temperatures of the glass

Sample	T_g (°C)	T_c (°C)	T_m (°C)	ΔT (°C)
G1	353.1	471.2	630.2	118.1
G2	352.8	470.1	680.4	117.3
G3	352.8	474.1	590.8	121.3

quantity of silver particles are primarily influenced by the composition of the glass. Fig. 5(a1) shows that the glass layer made from G1 glass powder contains numerous spherical silver nanoparticles, ranging in size from 10 to 200 nm. Fig. 5(b1) illustrates that the glass layer made from G2 glass powder contains many spherical silver nanoparticles of 10–100 nm and several irregular, silver microcrystals around 100 nm. Fig. 5(c1) reveals that the glass layer from G3 glass powder mainly consists of irregular, silver microcrystals ranging from 200 nm to 500 nm, with hardly any spherical silver nanoparticles. The variation in shape and quantity of silver particles can be attributed to the differing concentrations of silver atoms within the glass layer. During firing, once the glass begins to melt, the silver powder in the paste in contact with it starts to dissolve into the glass. The experiment indicates that the capacity to dissolve and precipitate silver is contingent on the glass composition. Consequently, with increasing TeO_2 content, the glass's capacity to dissolve silver diminishes, resulting in less silver within the glass and fewer spherical silver nanoparticles. However, higher TeO_2 content also encourages the formation of larger, irregular elongated silver microcrystals within the glass layer. Conversely, it was observed that the glass layer formed by G3 glass powder is thinner compared to those of G1 and G2. The reason is that G3, during the firing process, has a higher melting temperature and poorer high-temperature flowability, hindering its ability to flow through the silver powder gaps to the Ag–Si interface. This limitation could weaken the adhesion of the silver paste and the etching reaction of SiN_x on the silicon wafer surface.

Fig. 5(a2)–(c2) presents the SEM images of the front metallization of c-Si solar cells post HNO_3 etching. The HNO_3 solution removed the bulk silver layer, leaving behind the interfacial glass layer. Energy-dispersive spectroscopy (EDS) analysis confirmed that the white bright spots of varying shapes and sizes are silver, aligning with prior observations.[17,24,25] Fig. 5(a2)–(c2) correspond to samples C1, C2, C3, metallized

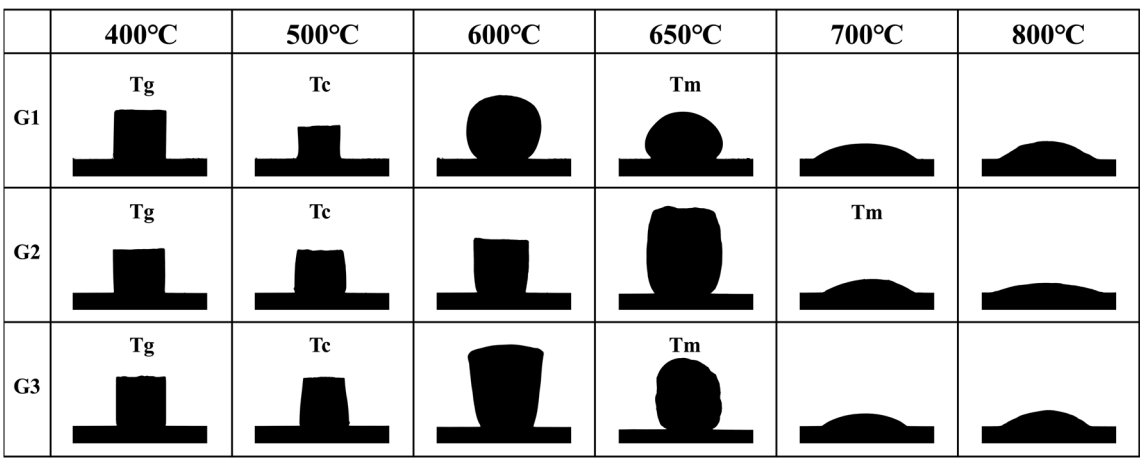

Fig. 3 Sample morphology of G1, G2 and G3 glass frits at 400–800 °C.

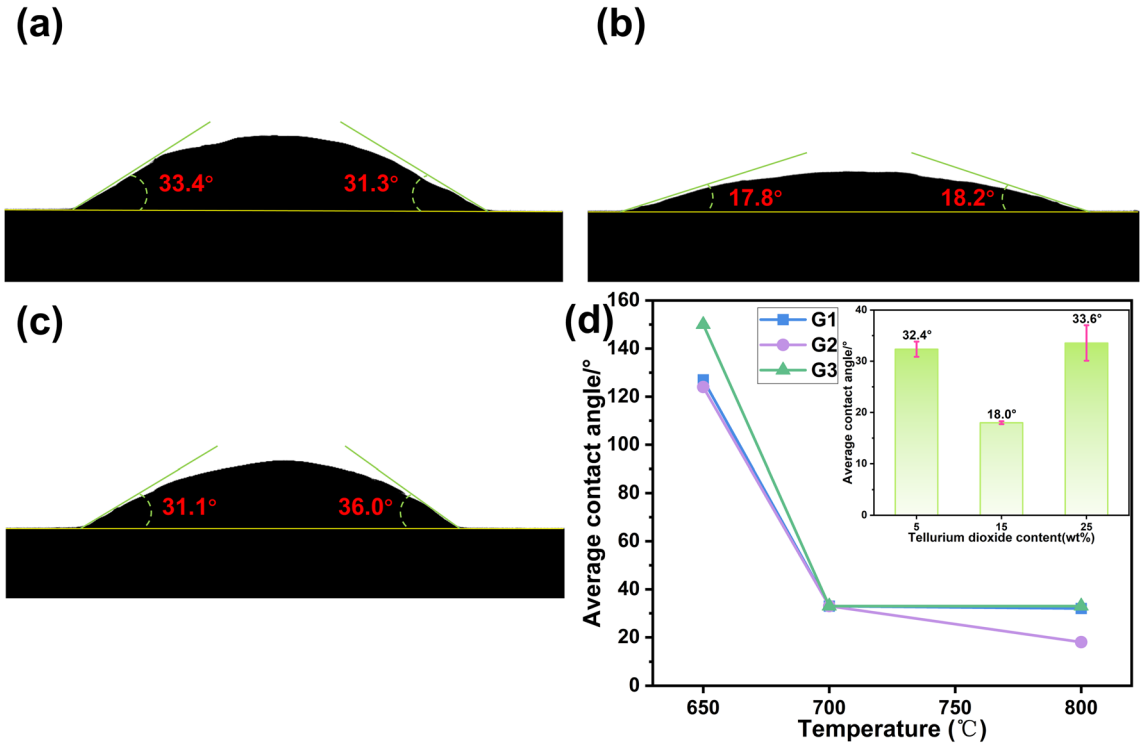

Fig. 4 Contact angle between different glass frits and silicon wafer after completely melting at 800 °C: (a) G1 glass frit; (b) G2 glass frit; (c) G3 glass frit, (d) the relationship between the contact angle of different glasses at melting temperature and temperature and the average contact angle of different glasses after full melting at 800 °C.

with silver pastes P1, P2, P3 derived from glasses G1, G2, G3, respectively. Fig. 5(a2) shows that the glass layer is unevenly distributed and fails to completely cover the pyramidal texture of the silicon surface. This is because G1 glass powder exhibits poorer wettability on the silicon wafer. The glass layer and the pyramidal silicon surface contain numerous 10–100 nm silver nanoparticles, with voids also present, as marked by yellow arrows in Fig. 5(a2). These voids are speculated to result from nitrogen gas released from the high-temperature reaction of glass with SiN_x on the silicon surface, which is difficult to escape due to the glass's high viscosity at high temperatures.[14,26] Fig. 5(b2) reveals a more evenly distributed glass layer, fully covering the silicon surface's pyramidal texture, and containing numerous 10–100 nm silver nanoparticles and chunky silver microcrystals (shown by green arrows). Furthermore, there are fewer bubbles in the glass layer compared to Fig. 5(a2), aligning with G2 glass's superior high-temperature flowability. In Fig. 5(c2), the glass layer is evenly distributed and completely covers the silicon surface's pyramidal texture. No silver nanoparticles are present in the glass layer, but larger silver microcrystals (shown by green arrows) are visible, and the glass layer contains fewer bubbles.

Fig. 5(a3)–(c3) displays the SEM images of samples C1, C2, C3 after HNO_3 etching to remove the bulk silver layer, followed by hydrofluoric acid etching to remove the glass layer. These images reveal the metallized pyramidal texture of the Ag–Si interface on the silicon layer surface. Energy-dispersive spectroscopy (EDS) analysis confirmed that the white particles, varying in shape and size, are silver. Fig. 5(a3) shows silver nanoparticles embedded in the pyramidal texture of the silicon surface, with the pyramid surfaces being relatively rough, which is a departure from previous studies.[14,16,27] This roughness could be attributed to excessive high-temperature etching of the silicon wafer by the glass, leading to deeper cavities and diminished surface smoothness. Fig. 5(b3) illustrates the silicon surface's pyramidal texture embedded with numerous 10–100 nm silver nanoparticles, and irregularly shaped, larger silver microcrystals at the pyramid tips (shown by green arrows). Energy-dispersive spectroscopy (EDS) was further applied to analyze the red boxed area in Fig. 5(d), reconfirming that the white particles and chunks on the silicon surface are silver, and additionally detecting traces of Te. This implies that Te serves as a connecting phase between Ag and Si, promoting the growth of silver microcrystals on the silicon emitter surface. Fig. 5(c3) shows that the pyramid tips on the silicon surface feature irregularly shaped, larger silver microcrystals (shown by green arrows), with almost no silver nanoparticles observed.

The experimental analysis reveals that improved high-temperature flowability and wettability of the glass facilitate its movement through the silver powder gaps towards the Ag–Si interface during sintering, resulting in an evenly spread glass layer. Additionally, with increasing TeO_2 content in the glass, its capacity to dissolve and precipitate silver gradually diminishes. When the TeO_2 proportion is low, numerous silver nanoparticles precipitate in the glass layer. As the TeO_2 content increases, the number of silver nanoparticles decreases, while

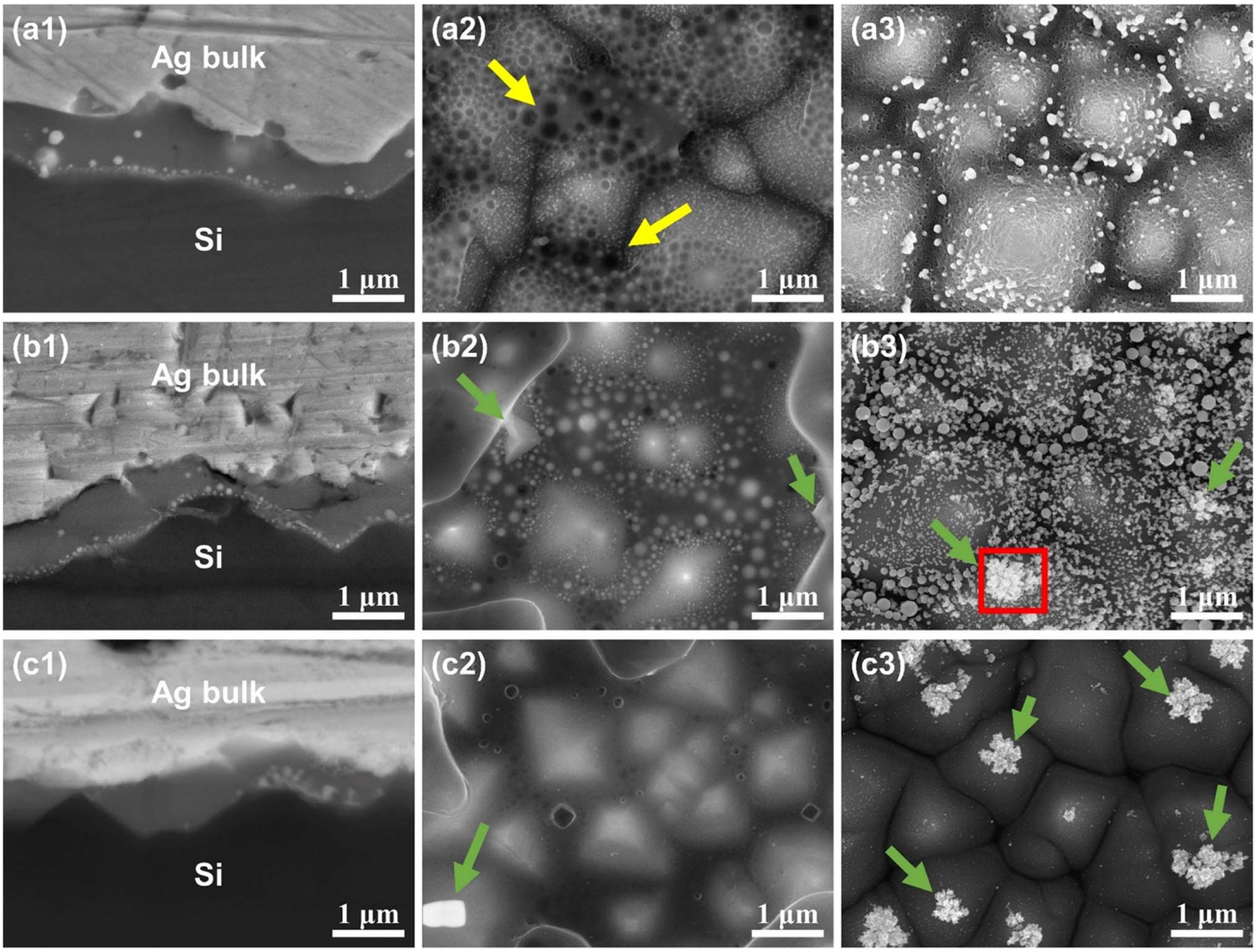

(d)

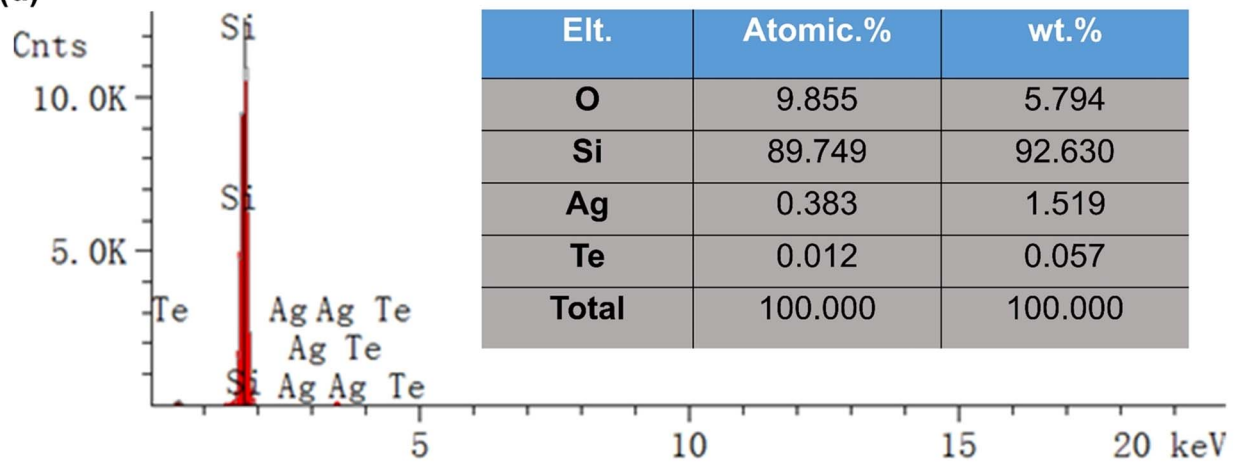

Elt.	Atomic.%	wt.%
O	9.855	5.794
Si	89.749	92.630
Ag	0.383	1.519
Te	0.012	0.057
Total	100.000	100.000

Fig. 5 (a1) SEM image of longitudinal section of sample C1, (a2) SEM image of sample C1 after HNO_3 etching (the yellow arrows are voids), (a3) SEM image of sample C1 after etching glass layer by HF acid, (b1) SEM image of longitudinal section of sample C2, (b2) SEM image of sample C2 after HNO_3 etching (the green arrows are silver microcrystals and the red box region was analyzed by EDS), (b3) SEM image of sample C2 after etching glass layer by HF acid (the green arrows are silver microcrystals), (c1) SEM image of longitudinal section of sample C3, (c2) SEM image of sample C3 after HNO_3 etching (the green arrows are silver microcrystals), (c3) SEM image of sample C3 after etching glass layer by HF acid (the green arrows are silver microcrystals), (d) energy dispersion spectroscopic analysis of the red box region in (b3).

the number of irregular silver microcrystals on the silicon surface's pyramid texture rises. The ohmic contact at the Ag–Si interface is established through the collective electrical conduction of these particles within the glass layer. Consequently, the composition of the glass significantly impacts the method of current transmission at the Ag–Si interface.

Previous studies identify two primary current transmission paths in the glass layer at the Ag–Si interface: direct current transmission *via* silver microcrystals and particles, and tunneling electron transmission at the interface of a thinner glass layer.[16,17] Fig. 6(a1)–(c1) show the schematic models of the Ag–Si interface current transmission paths formed by the three types of glass powders used in this study. In these models, green represents pyramidal silicon emitters, silver spheres represent silver nanoparticles, irregular silver chunks symbolize silver microcrystals, and black arrows depict the electron transmission paths. The theoretical band diagrams, based on the current transmission path models of these three glass powders, are illustrated in Fig. 6(a2)–(c2), depicting electron flow from right to left towards the Ag bulk.

Fig. 6(a1) illustrates the current transmission model for G1 glass powder, where electrons directly transfer from the Si emitter to the Ag bulk *via* numerous silver nanoparticles and tunneling through the thinner glass layer. Owing to the interface between the glass layer, silicon, and Ag bulk, the energy bands are slightly elevated in Fig. 6(a2), indicating that electrons need to overcome small barriers on both sides of the glass layer to reach the Ag bulk. Additionally, the abundance of silver nanoparticles in the glass layer facilitates direct electron transmission, meanwhile enhancing the path and probability of electron tunneling. Fig. 6(b1) shows the current transmission model for G2 glass powder, where electrons transfer to the Ag bulk *via* tunneling in the thin glass layer among silver nanoparticles and directly through the silver microcrystals on the emitter. Fig. 6(b2) indicates that the silver microcrystals on the emitter lower the electron transfer barrier, and the abundance of silver nanoparticles in the glass layer ensures efficient electron transfer, enhancing current transmission at the Ag–Si interface. Fig. 6(c1) depicts the current transmission model for G3 glass powder, where electrons transfer exclusively through the silver microcrystals on the emitter. Fig. 6(b2) illustrates that while the abundance of silver microcrystals on the emitter reduces the electron transfer barrier, the scarcity of silver nanoparticles in the glass layer and the

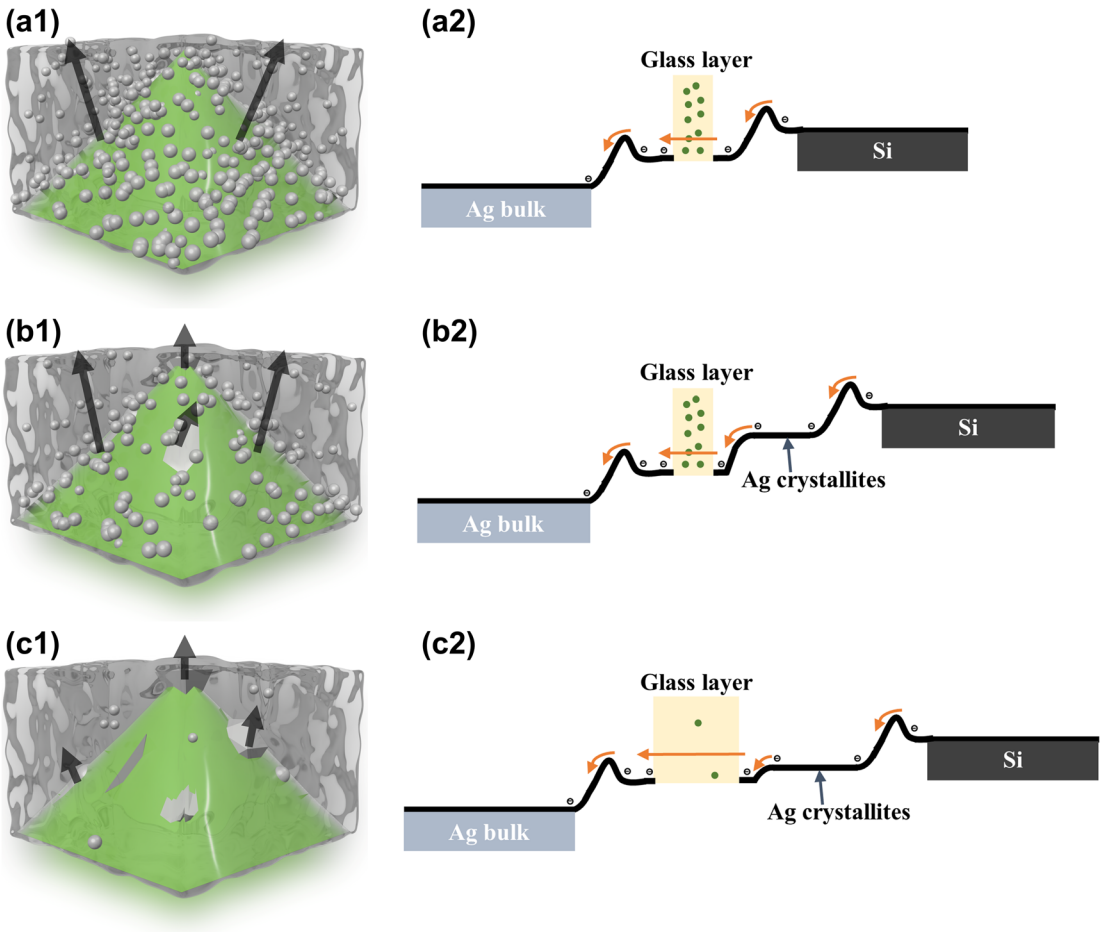

Fig. 6 (a1) Schematic model of Ag–Si interface current transmission path formed by G1 glass, (b1) schematic model of Ag–Si interface current transmission path formed by G2 glass, (c1) schematic model of Ag–Si interface current transmission path formed by G3 glass, (a2)–(c2) energy band diagrams of the corresponding electron transport paths. (The black arrow in (a1)–(c1) indicates the current transmission path).

Table 3 The electrical performance data for three pastes

Sample	R_c (mΩ cm^2)	V_{oc} (V)	I_{sc} (A)	FF (%)	Eta (%)	R_s (mΩ)	R_{sh} (Ω)
P1	1.7	0.6853	13.61	81.31	23.09	1.44	740
P2	1.5	0.6868	13.63	81.61	23.17	1.41	1051
P3	2.6	0.6866	13.55	81.11	23.03	1.67	1063

thicker gap diminish the probability of electron tunneling, impacting current transmission efficiency at the Ag–Si interface.

To compare the electrical performance of interface current transmissions formed by G1, G2, and G3 glass powders, we utilized screen printing pastes P1, P2, and P3, designed using the Transmission Line Model (TLM) method.[28,29] Following sintering, the resistance between silver electrodes was measured with a digital DC resistance meter to determine the contact resistance R_c. Concurrently, c-Si solar cell samples were fabricated using pastes P1, P2, and P3, and their *I–V* properties, including conversion efficiency (Eta), open-circuit voltage (V_{oc}), fill factor (FF), and short-circuit current (I_{sc}), were characterized using a Halm tester. The aforementioned data were compiled and summarized in Table 3.

The results show that the series resistance of P3 paste samples is significantly higher than that of P1 and P2, leading to the lowest short-circuit current and conversion efficiency. As mentioned earlier, the poor high-temperature flowability of G3 glass results in more residual glass in the Ag bulk, increasing its resistance. Additionally, the glass layer formed by G3 glass powder exhibits lower current transmission efficiency at the Ag–Si interface, leading to increased contact and series resistance. The shunt resistance of P1 is significantly lower compared to P2 and P3, resulting in a lower open-circuit voltage. This lower voltage can be attributed to G1 glass's excessive etching of the silicon wafer surface at high temperatures, damaging its p–n junction and leading to a lower conversion efficiency than P2. Consequently, owing to the excellent thermal properties and interfacial contact performance of G2 glass, paste P2 achieves the highest conversion efficiency.

4. Conclusions

This study explores the impact of the TeO_2–Bi_2O_3–B_2O_3 systems lead-free glass composition on high-temperature flowability, silicon wafer wetting, growth of silver microcrystals on silicon emitters, and formation of silver particles in the interfacial glass layer. The results indicate that with a TeO_2 to Bi_2O_3 mass ratio of 3 : 10, the lead-free glass demonstrates optimal high-temperature flowability and silicon wafer wettability, leading to the formation of an excellent interfacial contact glass layer during the sintering of photovoltaic silver paste. Our detailed study revealed that increasing TeO_2 content in the glass reduces its ability to dissolve and precipitate silver, consequently diminishing the current transmission efficiency of the Ag–Si interfacial glass layer. However, with a TeO_2 to Bi_2O_3 mass ratio of 1 : 12, the excess Bi_2O_3 reacts excessively with silicon, damaging the wafer's p–n junction and lowering photoelectric conversion efficiency. Moreover, the excess Bi_2O_3 and scarcity of TeO_2 in the glass layer hinder the growth of irregular silver microcrystals on the silicon emitter, reducing interface current transmission paths. Therefore, we determined that the optimal current transmission method at the Ag–Si interface is the combined action of silver microcrystals on the emitter and numerous silver nanoparticles in the glass layer. The best glass powder formulation is G2. The optimal interface contact resistance achieved with this formulation is 1.5 mΩ cm^2, while the minimum series resistance for the c-Si solar cell is 1.41 mΩ. This study provides new research thought into enhancing the current transmission efficiency of high-temperature silver paste in solar cells from the perspective of glass powder composition.

Conflicts of interest

Author Weichao Li was employed by the company R&D Center of Yunnan Tin Group (Holding) Co., Ltd.; author Junpeng Li was employed by the company Sino-Platinum Metals Co., Ltd. The remaining authors declare that they have no known competing financial interests or personal relationships that could have influenced the work reported in this paper.

Acknowledgements

This research was funded by the National Natural Science Foundation of China, grant number 51771084; the Major Science and Technology Project of Yunnan Province, grant number 202102AB080008; the Science and Technology Projects of Yunnan Precious Metals Laboratory, grant numbers YPML-2022050207 and YPML-2023050206; Joint Project of Enterprise Basic Research and Application Basic Research in Yunnan Province, grant number 202101BC070001-017.

References

1 A. Gommeringer, U. Schmitt-Radloff, P. Ninz, F. Kern, F. Klocke, S. Schneider, M. Holsten and A. Klink, *Procedia CIRP*, 2018, **68**, 22–27.
2 Y. Zhao, L. Y. Yang, D. Liu, J. T. Hu, L. Han, Z. J. Wang and F. Pan, *ACS Appl. Mater. Interfaces*, 2018, **10**, 1672–1677.
3 H. Elsayed, H. Javed, A. G. Sabato, F. Smeacetto and E. Bernardo, *J. Eur. Ceram. Soc.*, 2018, **38**, 4245–4251.
4 J. F. Zhang, X. J. Sun, H. Tong, Y. X. Yang, X. Yuan and H. B. Li, *J. Mater. Sci.: Mater. Electron.*, 2021, **32**, 6778–6787.
5 Z. Gao, X. Jiang, X. B. Wang, Y. J. Chen, J. Liu, H. B. Chen, Y. Lin and F. Pan, *Funct. Mater. Lett.*, 2019, **12**, 1950080.
6 J. F. Zhang, H. Tong, X. J. Sun, G. Q. Li, H. Li, Y. X. Yang, X. Yuan, C. Liu and H. B. Li, *J. Mater. Sci.: Mater. Electron.*, 2020, **31**, 5752–5759.

7 Q. Ma, S. H. Ma, J. T. Bai and H. Wang, *RSC Adv.*, 2017, **7**, 47500–47506.
8 S. Watanabe, T. Kodera and T. Ogihara, *J. Ceram. Soc. Jpn.*, 2016, **124**, 218–222.
9 K. R. Mikeska, M. J. Lu and W. L. Liao, *Prog. Photovoltaics*, 2019, **27**, 1071–1080.
10 C. T. Cui, T. Nie, S. Y. Ning, B. Zhou, G. Wang, S. H. Ma and H. Wang, *Sol. Energy Mater. Sol. Cells*, 2022, **235**, 111465.
11 Y. H. Sun, H. B. Xue, C. Q. Yang, Y. X. Tian, S. Y. Ning, S. H. Ma and H. Wang, *Sol. Energy Mater. Sol. Cells*, 2023, **253**, 112214.
12 Y. Kim, T. Nakayama and H. Kim, *J. Alloys Compd.*, 2020, **829**, 154500.
13 J. H. Kim, H. Y. Koo, Y. N. Ko and Y. C. Kang, *J. Alloys Compd.*, 2010, **497**, 259–266.
14 J. L. Zhang, J. C. Zhou, J. Huang and B. W. Lv, *Sol. Energy Mater. Sol. Cells*, 2022, **238**, 111585.
15 A. Kalio, M. Leibinger, A. Filipovic, K. Kruger, M. Glatthaar and J. Wilde, *Sol. Energy Mater. Sol. Cells*, 2012, **106**, 51–54.
16 B. W. Feng, Y. P. Liu, W. Chen, G. G. Xing, X. Q. Chen and X. L. Du, *Sol. Energy Mater. Sol. Cells*, 2023, **257**, 112381.
17 E. Cabrera, S. Olibet, D. Rudolph, E. Wefringhaus, R. Kopecek, D. Reinke and G. Schubert, *IEEE J. Photovoltaics*, 2013, **3**, 102–107.
18 C. H. Lin, S. Y. Tsai, S. P. Hsu and M. H. Hsieh, *Sol. Energy Mater. Sol. Cells*, 2008, **92**, 1011–1015.
19 S. Y. Ning, C. Q. Yang, S. Y. Li, J. T. Bai, H. Wang and S. H. Ma, *Sol. Energy Mater. Sol. Cells*, 2022, **244**, 111814.
20 A. Khanna, P. K. Basu, A. Filipovic, V. Shanmugam, C. Schmiga, A. G. Aberle and T. Mueller, *Sol. Energy Mater. Sol. Cells*, 2015, **132**, 589–596.
21 P. Ferrada, C. Portillo, V. del Campo, E. Cabrera, D. Rudolph, M. P. Bustos, M. J. Kogan and R. Kopecek, *IEEE J. Photovoltaics*, 2017, **7**, 727–734.
22 P. Ferrada, C. Portillo, E. Cabrera, R. Kopecek, M. Poncebustos, M. J. Kogan, V. Del Campo and E. Fuentealba, *J. Chil. Chem. Soc.*, 2015, **60**, 2905–2910.
23 M. Udovic, M. Valant and D. Suvorov, *J. Am. Ceram. Soc.*, 2004, **87**, 591–597.
24 E. Cabrera, S. Olibet, J. Glatz-Reichenbach, R. Kopecek, D. Reinke and G. Schubert, *Energy Procedia*, 2011, **8**, 540–545.
25 C. Ballif, D. M. Huljic, G. Willeke and A. Hessler-Wyser, *Appl. Phys. Lett.*, 2003, **82**, 1878–1880.
26 J. Y. Huh, K. K. Hong, S. B. Cho, S. K. Park, B. C. Lee and K. Okamoto, *Mater. Chem. Phys.*, 2011, **131**, 113–119.
27 P. Padhamnath, A. Khanna, N. Balaji, V. Shanmugam, N. Nandakumar, D. Wang, Q. Sun, M. Huang, S. M. Huang, B. B. Fan, B. B. Ding, A. G. Aberle and S. Duttagupta, *Sol. Energy Mater. Sol. Cells*, 2020, **218**, 110751.
28 P. N. Vinod, *J. Mater. Sci.: Mater. Electron.*, 2011, **22**, 1248–1257.
29 D. Y. Shin, S. S. Yoo and J. Y. Seo, *Int. J. Precis. Eng. Manuf. - Green Technol.*, 2015, **2**, 237–244.